Phase defects and spatiotemporal disorder in traveling-wave convection patterns

A. La Porta and C. M. Surko
Department of Physics, University of California, San Diego, La Jolla, California 92093
(Received 16 January 1997; revised manuscript received 23 April 1997)

Spatiotemporal disorder is studied in traveling-wave convection in ethanol-water mixtures. Spectral measures of disorder, linear correlation functions, and mutual information are used to characterize the patterns, and are found to give a weak indication of the level of disorder. The calculation of the complex order parameter for experimental patterns is described. It is found that the ordering of the patterns is accompanied by a dramatic change in the topological structure of the order parameter. Specific arrangements of defects are found to be associated with the elements of traveling-wave patterns, and the net charge and total number of defects is introduced as a measure of disorder in the patterns. The coarsening of the patterns is marked by an accumulation of net charge and a dramatic decrease in the number of defects. The physical significance of the defects is discussed, and it is shown that the phase velocity of the waves is lower in the vicinity of the defects. The defect-defect correlation functions are calculated for the convection patterns. It is shown that the ordering of the patterns is closely related to the apparent defect-defect interactions. [S1063-651X(97)01809-6]

PACS number(s): 47.54.+r, 47.27.Te, 47.52.+j

I. INTRODUCTION

In a spatially extended system which is driven far from equilibrium, a change in the strength of the forcing parameter or in the other physical parameters can cause an initially homogeneous system to become unstable to a spatial modulation [1]. The resulting breaking of translational symmetry and formation of a pattern can be an important influence on the physical properties of the system, such as energy, material, or momentum transport. Examples are as diverse as the formation of convection rolls in a fluid layer heated from below [2], the formation of chemical waves in a reaction-diffusion system [3] the self-organization of a colony of amoeba [4,5], or the excitation of transverse spatial structure in a large aperture laser [6–8].

Whereas patterns in equilibrium systems are constrained by a free-energy minimization principle and typically exhibit relaxational dynamics, patterns in nonequilibrium systems are free from this constraint and can exhibit complicated nonrelaxational dynamics. Under some circumstances, particularly when driven only slightly beyond their primary instabilities, patterns in nonequilibrium systems can be highly ordered, consisting of a regular pattern with a small number of defects. Under these circumstances, it is often the case that the patterns are universal and are determined by the symmetries of the system [1]. When driven farther beyond their primary instabilities, nonequilibrium systems often exhibit spatiotemporal disorder, in which the physical variables vary in time and space in a complicated manner. In some systems, this spatiotemporal disorder takes the form of the complicated evolution of an amplitude field, and the behavior of the system is naturally described in terms of the dynamics of this field [9–11]. In other cases, coherent structures or defects in the pattern appear to take a primary role, and a description of the system can be made in terms of the dynamics and interactions of these structures [12–14].

A variety of mathematical models have been introduced to describe patterns and spatiotemporal chaos in physically extended nonequilibrium systems. These include models which exhibit amplitude chaos [15,16] as well as defect-mediated chaos [6,17,18]. In the latter case, the statistics of phase defects have been used as an indicator of disorder in chaotic patterns [19]. It has also been found that the topological structure of the defects can place significant constraints on the properties of the patterns [20]. While it would be interesting to apply these ideas to the analysis of experimental systems, it is difficult to develop robust and accurate algorithms for locating defects in experimental patterns.

In this paper, we present a study of traveling-wave convection in a mixture of ethanol and water. We describe a transition from a pattern exhibiting intense defect-mediated disorder to a highly ordered pattern consisting of large domains of traveling waves separated by domain boundaries. We find that the spectral properties and amplitude correlations of the patterns give a weak indication of disorder in the patterns. By calculating the complex order parameter of the convection pattern, we show that it is possible to identify and track the trajectories of phase defects in the convection patterns with high accuracy. The statistics and dynamics of these defects are found to be a much more effective measure of disorder in the patterns. We calculate the defect-defect correlation functions and show that, to some extent, the coarsening of the pattern can be understood in terms of the dynamics and interactions of the defects.

II. CONVECTION IN ETHANOL-WATER MIXTURES

Rayleigh-Bénard convection in a mixture of ethanol and water is an example of double diffusive convection. In this system, there are two quantities—heat and ethanol concentration—which induce density fluctuations and can drive the convective flow. A thin layer of fluid, having average ethanol concentration c, is confined between two plates separated by a distance h. The plates are impenetrable to both components of the fluid and have a much larger thermal conductivity than that of the fluid mixture. The dimensionless forcing parameter is the Rayleigh number

$$\mathrm{Ra}=\frac{g\alpha h^3\Delta T}{\nu\kappa}, \tag{1}$$

where g is the acceleration of gravity, ν is the kinematic viscosity, κ is the thermal diffusion coefficient, α is the thermal expansion coefficient, and ΔT is the temperature difference imposed on the fluid layer. Ethanol-water mixtures are distinguished by having a strong Soret effect. The transport of ethanol concentration in the mixture is given by

$$\mathbf{j}_c=-D_c\boldsymbol{\nabla}c+D_cS_tc(1-c)\boldsymbol{\nabla}T+\mathbf{u}c, \tag{2}$$

where $\mathbf{j}_c$ is the ethanol concentration flux, $\mathbf{u}$ is the fluid velocity, D_c is the ethanol diffusivity and S_t is the Soret coefficient [21,22]. The first and third terms on the right side of Eq. (2) are the diffusion and advection terms, but the second term is a cross-diffusion term, and indicates that a concentration flux arises from a temperature gradient. Below onset, $\mathbf{u}=0$, and, when a temperature difference is applied to the fluid layer, the concentration gradient builds up until a steady state is reached for which $\mathbf{j}_c=0$.

Above the onset, the convective flow transports both heat and ethanol concentration, resulting in a complicated interplay of the temperature, concentration, and velocity fields. The coupling between the thermal and concentration density gradients is the separation ratio

$$\psi=-S_tc(1-c)\frac{\beta}{\alpha}, \tag{3}$$

where $\beta=\rho^{-1}(\partial\rho/\partial c)_T$ is the concentration expansion coefficient. A negative value of ψ indicates that the concentration density gradient opposes the thermal density gradient, and tends to stabilize the fluid layer against thermal convection.

The nature of the quiescent state is specified by Ra and ψ, but the onset and the dynamical properties of convection also depend on the relationships between the relevant diffusive time scales in the system. The Prandtl number $\mathrm{Pr}=\nu/\kappa$ relates momentum diffusion to heat diffusion, and influences the onset of secondary instabilities. The Lewis number $\mathcal{L}=D_c/\kappa$ relates concentration diffusion to heat diffusion, and is important in determining the onset and dynamics of the convective state. For small $\mathcal{L}$ and sufficiently negative values of ψ, the onset of convection is a Hopf bifurcation to a state of oscillatory convection in which the convection rolls rock back and forth, rather than overturn steadily [23–25].

The experiments described in this paper were performed in a mixture of 8% ethanol (by weight) in water at an average temperature of 26 °C, for which $\psi=-0.24$, $\mathrm{Pr}=12$, and $\mathcal{L}=10^{-2}$ [26]. A schematic bifurcation diagram for this mixture is shown in Fig. 1. Because of the large negative value of ψ and the strong separation of time scales for mass and thermal diffusion in this mixture, the Hopf bifurcation at r_{co} is strongly subcritical and the amplitude of the oscillatory convection grows until large-amplitude traveling-wave (TW) convection is triggered. In the TW state, the convection rolls overturn continuously, but propagate at a well-defined phase velocity [27–29]. TW convection has been widely studied as a model of strongly nonlinear wave propagation, in which superpositions of wave components are unstable.

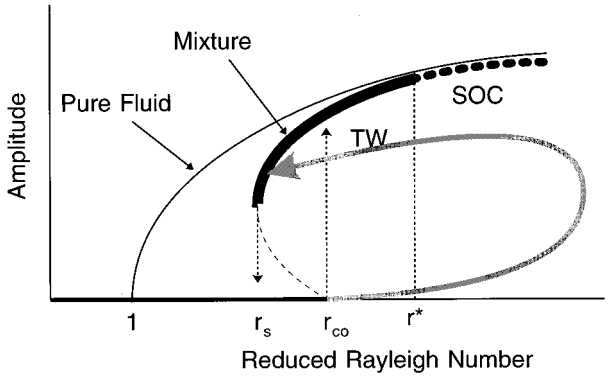

FIG. 1. Schematic bifurcation diagram for convection in a pure fluid and in a binary mixture with negative separation ratio. In the mixture, the heavy solid line indicates traveling-wave (TW) convection, and the heavy dashed line indicates stationary overturning (SOC) convection. Disordered states are initiated via the transient indicated by the gray arrow.

If the Rayleigh number is increased further after TW convection has been initiated, the phase velocity of the TW state decreases until a transition to stationary overturning convection is reached at $r^\star$ [30,31]. If the Rayleigh number is decreased, the phase velocity increases and TW convection remains stable until a saddle node bifurcation is reached at r_s. At this point, the finite amplitude convection state abruptly disappears. The measured values for the bifurcation points in the 8% mixture used here are $r_{co}=1.40$, $r_s=1.23$, and $r^\star=1.58$.

Patterns were studied in a cylindrical convection cell having a diameter of 21 cm and a height of 0.4 cm, with an aspect ratio $\Gamma=r/h$ of 26. The patterns are visualized using a white-light shadowgraph and recorded using a CCD camera and computer frame grabber. The results described below are expressed in terms of the characteristic time and distance scales of the system; distances are expressed in terms of the cell height $h=0.4$ cm, which sets the size of a convection roll, and times are expressed in terms of the vertical thermal diffusion time $\tau\equiv h^2/\kappa=124$ s. A description of the apparatus, as well as a survey of TW patterns in this system, has been published elsewhere [32].

III. DISORDER IN TW CONVECTION

In order to create a maximally disordered convection pattern, the Rayleigh number is rapidly increased from zero to a value of about 2.2, then quickly set to a value of 1.25 when the onset of convection is observed. This shock to the system, represented by the gray arrow in Fig. 1, produces an extremely disordered pattern which is composed of superpositions of wave components and small domains of traveling-waves. Such a pattern is shown in Fig. 2(a). Eventually, a highly ordered convection pattern forms in the cylindrical convection cell consisting of several large domains of traveling waves separated by slowly moving, well-defined domain boundaries. The ordered patterns always exhibit global rotation, with the rolls in all domains moving around the boundary of the convection cell in the same direction [32]. The direction of rotation varies from run to run, but, once

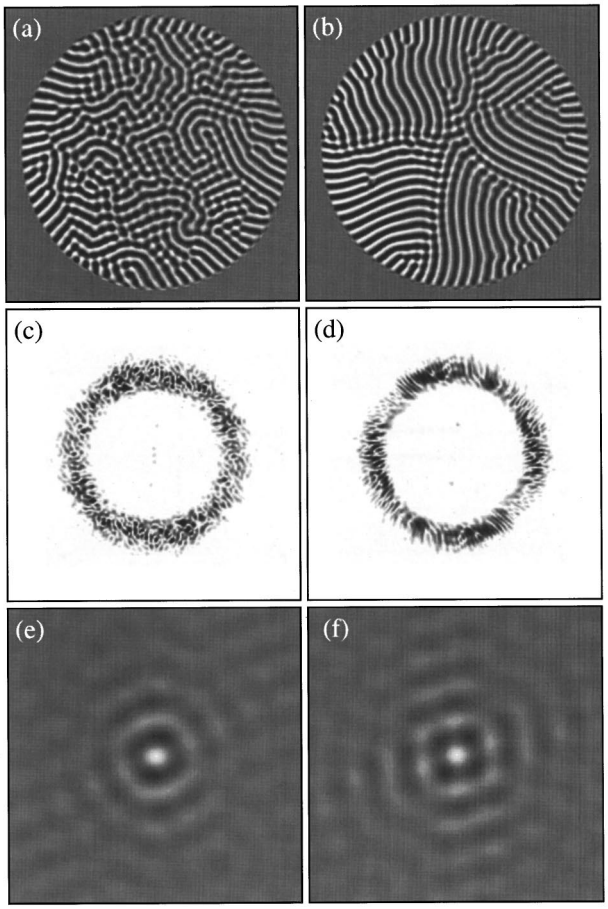

FIG. 2. (a) A TW convection pattern recorded at $r=1.27$, approximately 50τ after convection, was initiated by the procedure described in the text. (b) The pattern recorded 1950τ after convection was initiated. (c) The spatial Fourier transform of (a). (d) The spatial Fourier transform of (b). (e) The autocorrelation function of (a). (f) The autocorrelation function of (b).

established, never reverses itself. A typical ordered pattern is shown in Fig. 2(b).

The spatial Fourier spectra of the patterns in Figs. 2(a) and 2(b) are shown in Figs. 2(c) and 2(d). Both spectra have a characteristic ring shape, with the spectral energy concentrated at $|\mathbf{k}|\approx\pi$. On a fine scale, the spectrum of the disordered pattern has a granular appearance, whereas the spectrum of the ordered pattern is smoother and has a banded structure. On a coarser scale, the spectra are quite similar and exhibit a similar dependence on $|\mathbf{k}|$. In Figs. 2(e) and 2(f), the spatial autocorrelation functions are shown for the disordered and ordered patterns. The correlation functions both show a target pattern, which is typical for quasiperiodic images. The correlation function for the disordered pattern is nearly isotropic, whereas the correlation function for the ordered pattern exhibits clear anisotropy. This is because the correlation is stronger for displacement directions corresponding to the roll orientations in the large TW domains of the ordered pattern.

The coarsening of the convection pattern is accompanied by subtle changes in the spatial Fourier spectrum and the autocorrelation function, but these changes are less pronounced and no easier to quantify than the change in the pattern itself. An important issue is whether a simple scalar

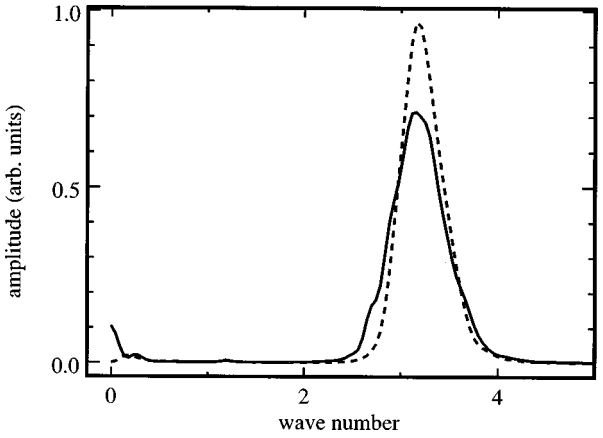

FIG. 3. Plot of the structure function, $S(k)$, of data shown in Figs. 2(c) (solid curve) and 2(d) (dotted curve). The wave number is in units of the inverse cell height h^{-1}.

measure of the disorder can be found. As a first step in this direction, the two-dimensional spectral distribution can be reduced to a function of $|\mathbf{k}|$, by integrating out the angular dependence using

$$S(k)=\frac{1}{2\pi}\int_0^{2\pi}P(k\,\cos\theta,k\,\sin\theta)\,d\theta, \tag{4}$$

where $P(k_x,k_y)$ is the power spectrum and $S(k)$ is called the structure function [11,13,33].

The structure functions calculated from the power spectra in Figs. 2(c) and 2(d) are shown in Fig. 3, where the normalization of $S(k)$ is arbitrary, but the same for both patterns. Fig. 3 reveals an increase in intensity and a slight sharpening of the wave number distribution as the pattern becomes ordered. A reasonable strategy is to evaluate the moments of the structure function as a measure of the level of disorder in the pattern. As will be discussed below, only a slight change in these moments is observed during the ordering of the pattern.

The angular dependence of the autocorrelation function can also be integrated out to obtain a radial correlation distribution,

$$\mathcal{C}(r)=\frac{1}{2\pi}\int_0^{2\pi}C(r\,\cos\theta,r\,\sin\theta)\,d\theta, \tag{5}$$

where $C(x,y)$ is the spatial correlation function. The length of the tail of the correlation function, or more practically, the height of the nth maximum (with $n>1$) may be used as an indicator of long-range order in the pattern. The radial correlation function, shown in Fig. 4, indicates a small increase in long-range order as the large domains form.

Having established that the structure function and radial autocorrelation functions are modified by the ordering of the patterns, we can use these quantities to track the coarsening of the pattern. The evolution of the pattern was recorded in 5400 video frames, over a period of 1960τ, and the Fourier transforms and correlation functions were calculated from each frame. In Fig. 5, the mean and standard deviation of the structure function $S(k)$ and the value of the third maximum of the radial correlation function, $\mathcal{C}(r)$, are plotted as a func-

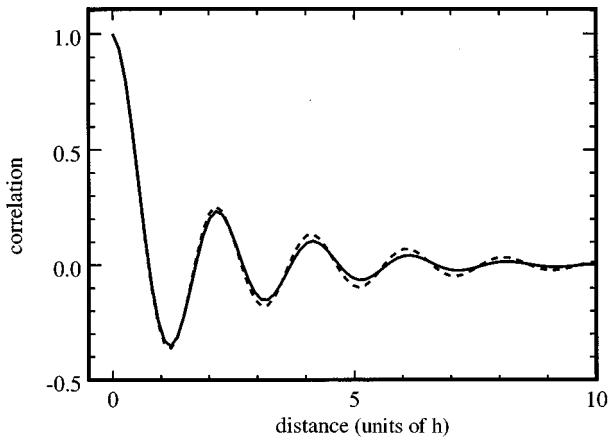

FIG. 4. Plot of the radial distribution, $C(r)$, of the autocorrelation functions in Figs. 2(e) (solid curve) and 2(f) (dotted curve) with the angular dependence integrated out. Distances are in terms of the cell height h.

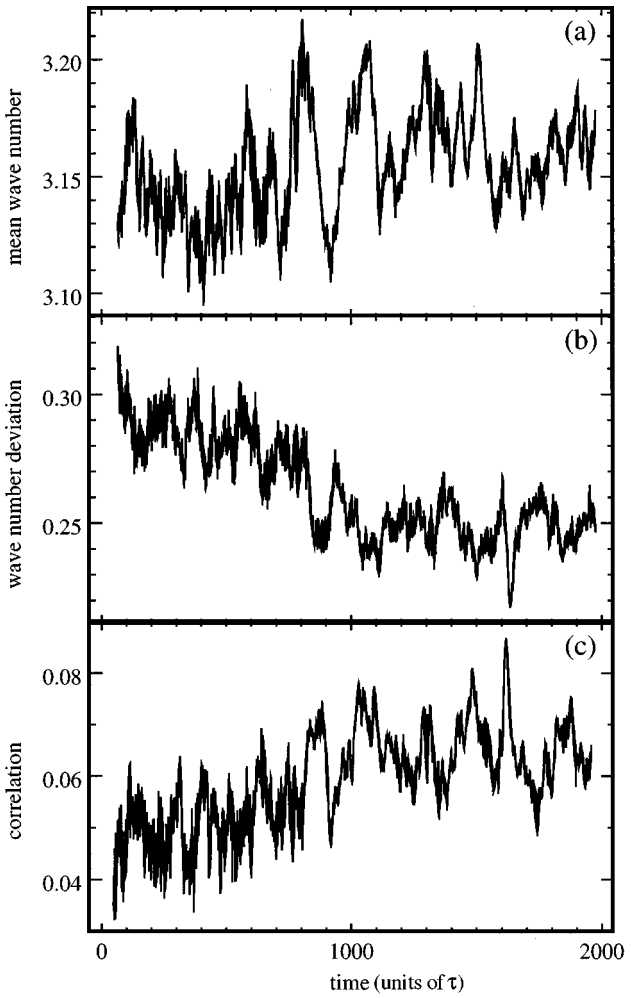

FIG. 5. The time series of the spectral measures of disorder of the TW convection pattern shown in Fig. 2. (a) The mean value of the structure function distribution. (b) The standard deviation of the structure function distribution. (c) The value of the third maximum of the radial autocorrelation function. The wave number is in units of the inverse cell height, h^{-1}, and time is in units of the vertical thermal diffusion time, τ.

tion of time. Fluctuations of $\pm 2\%$ are found in the mean wave number of the pattern, but no clear trend is evident. The width of the wave number distribution [Fig. 5(b)] narrows slightly, from 0.30 to 0.25, and the value of the radial correlation function (at a distance of $\approx 6h$ or $\approx 3\lambda$) increases from 0.045 to 0.062 [Fig. 5(c)], a change which is comparable to the noise in this measure.

To summarize the results of this section, the transition from disorder to order in the TW convection patterns is accompanied by discernible changes in the spectral distribution and the correlation amplitude of the patterns, but the changes in these measures are surprisingly weak in view of the dramatic change in the pattern between Figs. 2(a) and 2(b). Such a signal could easily be produced by a much less dramatic change in the pattern, such as a slight variation of the wave number within the large roll domains. It can be concluded that the patterns in Figs. 2(a) and 2(b) contain a continuum of spectral components concentrated at $|\mathbf{k}| \approx \pi$ and spanning a continuous spectrum of angles. In the disordered patterns, the individual spectral components span the entire pattern and overlap with each other, whereas in the ordered patterns, they are segregated in well-defined domains. The small changes in the measures in Fig. 5 are a side effect, rather than a direct result, of this qualitative change in the nature of the patterns.

The fact that the coarsening of the patterns is not reflected in the spectral properties of the system can also be interpreted as a failure of the linear paradigm in the analysis. If we interpret the pattern as arising from a PDE, the spectral components are independent if the nonlinear terms are neglected. In this case, the spectrum would tend to be excited according to the growth rates of the linearized system and the phases would be random. The tendency of the pattern to order itself, by partitioning itself into domains of traveling waves, is a manifestation of the coupling between these spectral components, which must arise from nonlinearities in the system. The ordering of the pattern then manifests itself in the development of complicated phase relationships among the Fourier components, rather than in the spectral amplitudes.

IV. AVERAGE MUTUAL INFORMATION

In the dynamical systems literature, the use of the correlation function is sometimes criticized because it measures only linear correlations between variables and ignores higher-order correlations. In view of the discussion above, it is not clear that linear correlations are the most appropriate measure of disorder in the TW patterns. Instead of looking for linear correlations in the images, we can ask a more general question: is the probability distribution for the intensity at a point in the image altered by the prior measurement of the intensity at a neighboring point?

Let us label the two variables A and B and their possible values a_j and b_k. (As applied to the patterns we are studying, A and B are the measurements of the pattern intensity at two points separated by a certain distance.) An expression for the amount of mutual information between these two measurements in terms of their joint probability distribution was derived by Shannon and Weaver [34]. The mutual information (in bits) between measurements a_j and b_k is given by

$$I_{AB}(a_j,b_k)=\log_2\left[\frac{P_{AB}(a_j,b_k)}{P_A(a_j)P_B(b_j)}\right], \tag{6}$$

where $P_A(a)$ and $P_B(b)$ are the probability distributions for A and B and $P_{AB}(a,b)$ is the joint probability distribution. If the two variables are independent, the measurement of the first variable gives no information about the second variable and the mutual information is zero. In this case, the joint probability distribution is of the form

$$P_{AB}(a,b)\equiv P_A(a)P_B(b), \tag{7}$$

and evaluation of Eq. (6) gives

$$I_{AB}(a,b)\equiv 0, \tag{8}$$

as expected. If two measurements, a_i and b_k, are totally correlated and a_i is measured, then the subsequent measurement of b_k gives no additional information. In this case the mutual information is large and, as expected, Eq. (6) attains its maximum value, which is of order $\log_2 n$, where n is the number of possible outcomes of A or B.

Order in a spatial pattern can be evaluated by determining how much information is obtained, on average, about a given pixel by measuring the value of a pixel which is offset by a certain distance [35,36]. This average mutual information is determined by evaluating

$$I(x,y)=\sum_{j,k} I_{AB}(a_j,b_k)P_{AB}(a_j,b_k), \tag{9}$$

where the summation is over all possible values of the pixel intensities A and B. In evaluating Eqs. (6) and (9), P_A and P_B are the probability distribution for the pixel intensity, averaged over the image, and P_{AB} is the joint probability distribution compiled from all pairs of pixels which are separated by the distance (x,y). In this context, Eq. (9) may be interpreted as a generalization of the linear correlation function, which, in terms of the joint probability distribution, is

$$C(x,y)=\frac{1}{\sigma_a\sigma_b}\sum_{j,k} a_j b_k P_{AB}(a_j,b_k), \tag{10}$$

where σ_a and σ_b are the standard deviations of the two variables. The function $I_{AB}(a_j,b_k)$ replaces for the factor $a_j b_k$ which appears in the linear correlation function.

The average pixel-pixel mutual information function for the images in Figs. 2(a) and 2(b) is shown in Fig. 6. The mutual information map is a target pattern and is qualitatively similar to the autocorrelation function, Figs. 2(c) and 2(d). The angular dependence of the mutual information function may be integrated out to obtain a radial distribution of mutual information, which is shown in Fig. 7. The results using mutual information seem qualitatively similar to those obtained from the linear correlation function, with the ordered patterns exhibiting an enhancement of mutual information at larger distances. The contrast between the ordered and disordered patterns seems to be somewhat more pronounced in the mutual information, indicating that it is a more sensitive measure of spatial disorder in the patterns studied here.

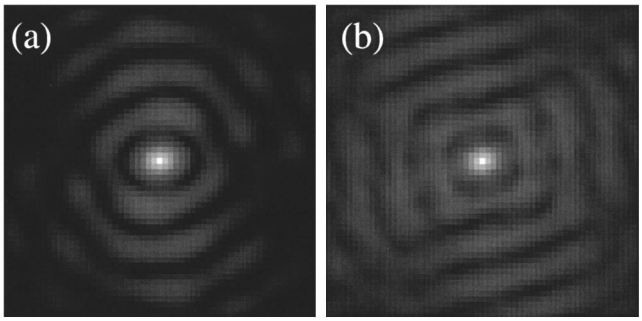

FIG. 6. Average pixel-pixel mutual information as a function of displacement for the patterns of Figs. 2(a) and 2(b). Black indicates zero mutual information, and white indicates maximum mutual information.

V. COMPLEX ORDER PARAMETER AND PHASE DEFECTS

In the previous sections, the level of spatial disorder in the convection patterns was measured in terms of the spectral content and in terms of two different measures of long-range order (linear correlation and mutual information). The ordering of the pattern is associated with a discernible change in these measures, shown in Figs. 3, 4, and 7; however, these measures do not appear to capture the essence of the coarsening process. In previous work, we have shown how the complex order parameter may be calculated in the TW patterns [32], and in this section we show that the level of disorder in the patterns can be described very effectively in terms of the topological structure of the order parameter.

A. Identification of phase defects

In the traveling-wave patterns observed in this experiment, the time series of each pixel in the video sequence is oscillatory, and the pattern can therefore be described as an ensemble of oscillators, one for each pixel. Taking this view, the specification of the pattern at a given time consists of the complex amplitude (modulus and phase) and oscillation frequency of each pixel. The modulus of the complex amplitude varies slowly in space and time and so the structure of the pattern is determined mainly by the phase relationships be-

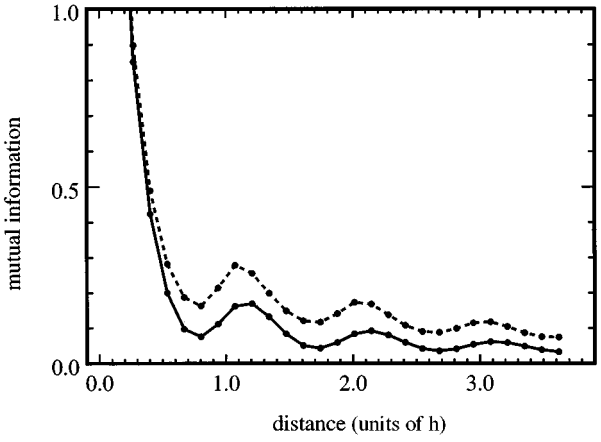

FIG. 7. Radial distribution of the mutual information from the data in Figs. 6(a) (solid curve) and 6(b) (dotted curve).

tween the pixels comprising the pattern. The rate of change of the pattern is closely related to the frequency field [32].

The complex amplitude and frequency fields can be calculated from the oscillatory pattern data by performing a complex demodulation of the time series of each pixel [37,38]. It is assumed that the time series of each pixel, $\alpha(\mathbf{x},t)$, has a narrow Fourier spectrum, centered at ω, and can be written in the form

$$\alpha(\mathbf{x},t)=\alpha_\omega(\mathbf{x},t)\cos[\omega t+\phi(\mathbf{x},t)], \tag{11}$$

where $\alpha_\omega(t)$ is the envelope and $\phi(t)$ represents a phase modulation with respect to the carrier frequency ω. Given the time sequence for each pixel, our goal is to calculate the two unknown functions $\alpha_\omega(\mathbf{x},t)$ and $\phi(\mathbf{x},t)$. The latter function is particularly important. When evaluated at a given time t_0, it indicates the relative phases of the oscillators representing the pattern at that time.

The functions $\alpha_w(\mathbf{x},t)$ and $\phi(\mathbf{x},t)$ are calculated as follows. The data sequence is first multiplied by a carrier wave $e^{i\omega t}$, where ω is chosen to match the observed spectral peak in the data. Dropping the explicit dependence on $\mathbf{x}$ from our notation, the transformed time series, $\mathcal{A}'(t)$, is

$$\begin{aligned}\mathcal{A}'(t)&=\alpha(t)e^{i\omega t}=\alpha_\omega(t)\cos[\omega t+\phi(t)](\cos\omega t+i\ \sin\omega t)\\&=\frac{\alpha_\omega(t)}{2}\{\cos[2\omega t+\phi(t)]+\cos[\phi(t)]\\&\quad+i\ \sin[2\omega t+\phi(t)]-i\ \sin[\phi(t)]\}.\end{aligned} \tag{12}$$

A low-pass filter is then applied to eliminate components with frequency greater than ω, leaving the near-dc terms $\cos[\phi(t)]$ and $\sin[\phi(t)]$. The resulting demodulated time series $\mathcal{A}(t)$ is

$$\begin{aligned}\mathcal{A}(t)&=\frac{\alpha_\omega(t)}{2}\{\cos[\phi(t)]-i\ \sin[\phi(t)]\}\\&=\frac{\alpha_\omega(t)}{2}e^{-i\phi(t)}.\end{aligned} \tag{13}$$

Examination of Eq. (13) reveals that the modulus of $\mathcal{A}(t)$ is the envelope function $\alpha_\omega(t)$ and that the complex phase of $\mathcal{A}(t)$ is the phase modulation of the original data, $\phi(t)$.

Although the experimental pattern is explicitly a real valued function (i.e., the intensity of the image as a function of time and space) it is convenient to consider it to be the real part of a complex order parameter, $A(\mathbf{x},t)$, defined by

$$\begin{aligned}\alpha(\mathbf{x},t)&=\mathrm{Re}[\mathcal{A}(\mathbf{x},t)e^{i\omega t}]\\&=\mathrm{Re}[A(\mathbf{x},t)],\end{aligned} \tag{14}$$

where Re indicates the real part. The time derivative of the pattern is then given by

$$\frac{d}{dt}\alpha(\mathbf{x},t)\approx\mathrm{Re}[i\omega\mathcal{A}(\mathbf{x},t)e^{i\omega t}], \tag{15}$$

where in taking the derivative, it has been assumed that $\mathcal{A}(\mathbf{x},t)$ varies slowly with time. In the TW patterns, the (unseen) imaginary part of the order parameter has a definite meaning, since it is closely related to the time derivative of the pattern and indicates the local direction of propagation of the waves. This complex field is closely related to the complex order parameter described by the complex Ginzburg-Landau equation, in which the temporal oscillation of the pattern corresponds to the rotation of the amplitude in the complex plane, and the spatial derivatives in the equation express the coupling between neighboring oscillators.

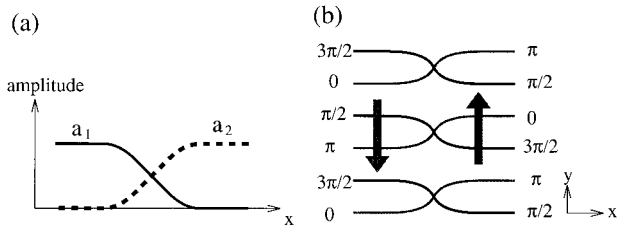

FIG. 8. (a) A sketch of the envelope functions which appear in Eq. (17). (b) The phase contours near a zipper boundary, where the arrows indicate the direction of propagation.

Within a domain of traveling waves, the complex order parameter is of the form

$$A(\mathbf{x},t)=A_0e^{i[\mathbf{k}\cdot\mathbf{x}-\omega t]}, \tag{16}$$

where ω is the oscillation frequency, and the wave vector $\mathbf{k}$ points in the direction of propagation. In this case, the phase of the order parameter is smooth and well defined everywhere. However, at a boundary between domains of traveling waves, there is an interface between regions with different wave vectors, and it is impossible for the two fields to connect smoothly. One example of such a domain boundary, observed in TW convection, is a configuration called a ''zipper.'' In a zipper, the rolls on either side of the domain boundary are perpendicular to the boundary, but propagate in opposite directions, in a configuration reminiscent of a shear flow [32,39,40]. The complex order parameter of the pattern near the boundary is a superposition of two wave components of the form

$$A(\mathbf{x},t)=a_1(x)e^{i(ky-\omega t)}+a_2(x)e^{i(-ky-\omega t)}, \tag{17}$$

where a_1 and a_2 are the envelopes of the waves, and the zipper is aligned along the x axis. Measurements indicate that the envelopes consist of a smooth crossover from one component to the other, where the cutoff distance is of the order of the pattern wavelength [41], as sketched in Fig. 8(a). Using Eq. (17) with this form for a_1 and a_2, it can easily be shown that the complex amplitude is equal to zero at a series of points with coordinates

$$x=0,\quad y=\frac{\pi}{2k},\frac{3\pi}{2k},\frac{5\pi}{2k},\ldots, \tag{18}$$

where the origin of x is defined such that $a_1=a_2$ at $x=0$. At these points, called phase defects, the contours of $\mathrm{Re}(A)=0$ and $\mathrm{Im}(A)=0$ intersect, and the phase of the complex amplitude is undefined. The phase contours at a zipper boundary are illustrated in Fig. 8(b). Writing the phase of the complex amplitude as ϕ, the integral of $d\phi$ on

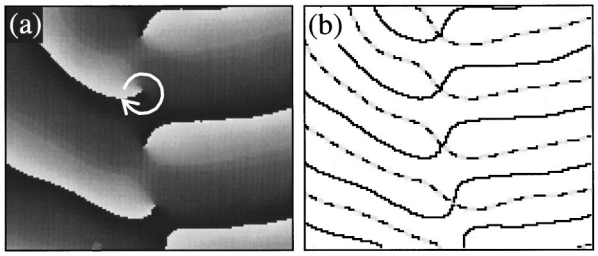

FIG. 9. Phase of the complex amplitude in a closeup view of a zipper taken from experimental data. (a) The phase ($0 \rightarrow 2\pi$) is mapped to gray scale (white→black). A 2π phase shift is accumulated around the circular arc shown. (b) Contours of $\mathrm{Re}(A)=0$ and $\mathrm{Im}(A)=0$, indicated by solid and dashed lines, intersect at the phase defects.

a closed path enclosing a defect is equal to $2\pi n$, where n is defined as the topological charge of the defect [42].

Figure 9(a) shows a high-resolution image of the complex order parameter calculated from a TW convection pattern containing a zipper boundary. Waves are moving upward on the left side of the boundary, and downward on the right side of the boundary. Several phase defects appear along the center line of the boundary. The circular arrow surrounding one defect indicates a path over which a 2π phase shift is accumulated, indicating that a defect of unity charge is contained therein. Contours of $\mathrm{Re}(A)=0$ and $\mathrm{Im}(A)=0$ are shown in Fig. 9(b), and are found to cross at the phase defects. Therefore, a zipper boundary manifests itself in the order parameter of the experimental patterns as a row of phase defects having the same unit topological charge and separated by a distance of π/k (half the pattern wavelength).

The results are similar for the case of a perpendicular boundary, for which

$$A(\mathbf{x},t)=a_1(y)e^{i(-ky-\omega t)}+a_2(y)e^{i(-kx-\omega t)}. \qquad (19)$$

In this case, a row of phase defects is obtained, but spaced by a distance $2\pi/k$, which is equal to the pattern wavelength. (In both the zipper and perpendicular boundaries, the number of defects is equal to the number of roll pairs which terminate at the domain boundary.) A closeup of a perpendicular boundary, in which rolls move downward from the top of the image and leftward along the bottom of the image, is shown in Fig. 10.

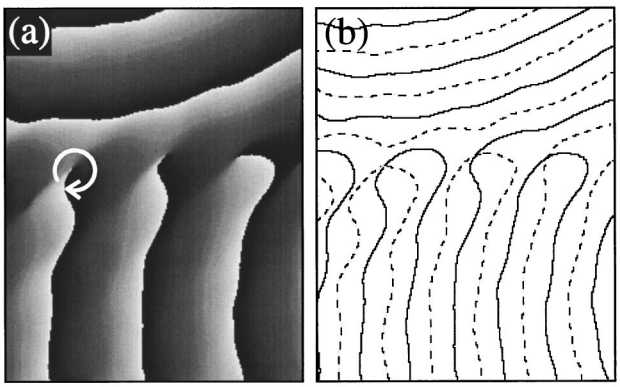

FIG. 10. Phase of the complex amplitude in a closeup view of a perpendicular boundary, as in Fig. 9.

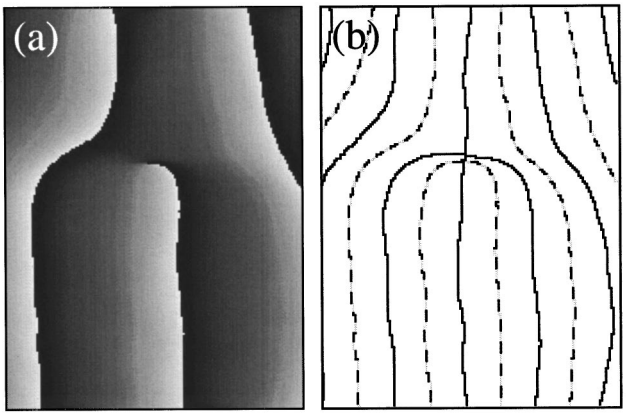

FIG. 11. Phase of the complex amplitude in a closeup view of a dislocation, as in Fig. 9.

We have identified two other structures which commonly appear in the TW convection patterns. The first is the simple dislocation, shown in Fig. 11, in which a single defect marks the termination of a roll. The second is the alternating ''cross-roll'' pattern [43], in which two mutually perpendicular standing waves alternate in time. (An instability somewhat similar to this occurs in stationary convection, in which a region of long-wavelength rolls becomes unstable to a set of perpendicular rolls with a shorter wavelength, as discussed in Ref. [2]). The complex amplitude of the cross-roll pattern is of the form

$$A(\mathbf{x},t)=a_1(\mathbf{x},t)e^{i(kx-\omega t)}+a_2(\mathbf{x},t)e^{i(-kx-\omega t)} +a_3(\mathbf{x},t)e^{i(ky-\omega t)}-a_4(\mathbf{x},t)e^{i(-ky-\omega t)}, \qquad (20)$$

where the envelopes $a_n(x,y,t)$ are nominally equal, but fluctuate in time and space. The time development of this field is shown in Fig. 12. Figure 13 shows data for an alternating cross-roll patch which is quite uniform on the upper-left side and merges into a domain of traveling waves toward the lower right. As may be determined from Eq. (20), or observed in Fig. 13, the cross-roll area contains alternating positive and negative defects on a square lattice with a lattice constant equal to π/k. The net charge of the cross-roll structure is therefore zero, although there are $(k/\pi)^2$ defects per unit area [44].

Given that specific structures in TW convection patterns are predicted to be marked by specific configurations of defects, and that the complex order parameter calculated from experimental patterns exhibits these structures, it is useful to design an algorithm that can automatically identify defects in the convection patterns with maximum efficiency and resolution. Figure 14 is a schematic diagram of the structure of a

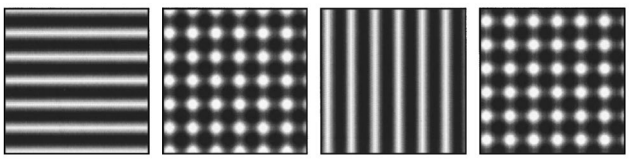

FIG. 12. Illustration of the temporal development of an alternating cross-roll pattern. The four panels are obtained by evaluating Eq. (20) with uniform and equal a_n at $t=\pi/4\omega$, $\pi/2\omega$, $3\pi/4\omega$, and π/ω.

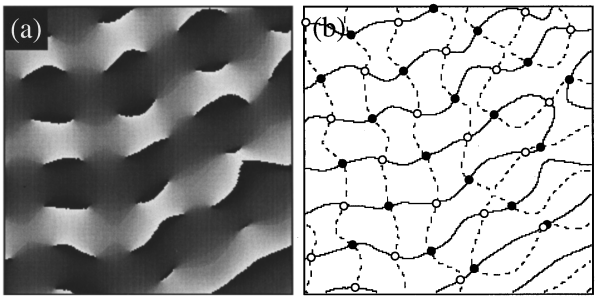

FIG. 13. Phase of the complex amplitude in a closeup view of a cross-roll pattern, as in Fig. 9. In (b) open (closed) circles represent phase defects of positive (negative) topological charge.

phase defect. In principle, a phase defect may be identified by integrating the phase $d\phi$ on a closed loop and checking for nonzero topological charge. In practice, the complex amplitude calculated from an experimental pattern is not continuous, but consists of values sampled on a discrete lattice of pixels, as illustrated schematically in Fig. 14(b). It is therefore not possible to calculate the topological charge from a discrete lattice with absolute certainty.

If we assume, for example, that for a circular integration path the phase of the complex amplitude varies with the polar angle as shown by the solid curve in Fig. 15 (which represents a topological charge of unity), then the values sampled on a discrete representation of the field [illustrated in Fig. 14(b)] would be represented by the gray circles on the curve in Fig. 15. However, the discrete representation of the dashed phase curve in Fig. 15 would be indistinguishable from the representation of the solid curve, despite the fact that the dashed curve represents a topological charge of zero, rather than unity. The trouble is that as we walk around the lattice and accumulate the total phase for the loop, there is an ambiguity, modulo 2π, as to the value of the phase increment on each step. The most natural assumption is to choose the phase increment with the smallest absolute value on each step (so $-\pi<\Delta\phi<\pi$).

In practice, the calculation of the topological charge is reliable as long as the typical phase difference between adjacent pixels is well below π. In order to satisfy this condition, the image sampling resolution must be high compared with the wave number of the pattern, and the number of steps in the loop must be sufficiently high to resolve the phase of the defect itself. The data presented here are sampled at a resolution of at least 14 pixels per wavelength, and the topological charge at each pixel is calculated using a loop consisting of the eight surrounding pixels. Under these conditions, the error rate is extremely low. In order to identify all defects in the pattern, the charge is calculated at each pixel, and recorded in a separate charge map. Generally, defects lie between pixels, and are contained by loops centered on four adjacent pixels, as indicated by the unshaded lattice points in Fig. 14(b). Therefore, we identify any connected group of pixels with the same nonzero topological charge as a single defect. This algorithm is capable of resolving a pair of defects as long as they are separated by at least one pixel.

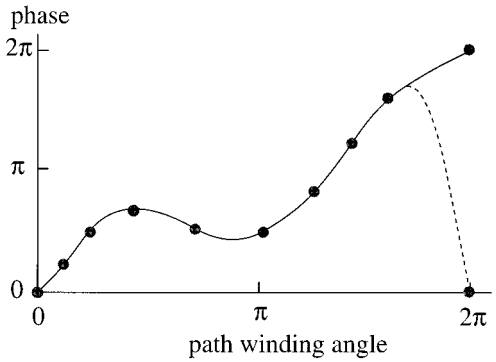

FIG. 15. Plot of the phase of the complex amplitude along a path surrounding the defect, illustrating possible ambiguity in identifying a phase defect in a discretely sampled image.

In Fig. 16, phase defects of unit positive and negative charge, identified using the algorithm described above, are marked by black and white dots for the two convection patterns shown in Fig. 2. The disordered pattern in Fig. 16(a) contains 436 positive defects and 416 negative defects, giving a total of 852 defects and a net charge of $+20$. The ordered pattern, shown in Fig. 16(b), contains 25 positive defects and 97 negative defects, for a total of 122 defects and a net charge of -72. The disordered convection pattern is evidently characterized by a large number of defects with no statistically significant net charge. The charge excess of 20 is less than that which would be expected if the 852 defects were randomly assigned a charge of ± 1. The ordered convection pattern, by contrast, is characterized by a much smaller number of defects, which are predominantly of the same sign. In all runs in which a disordered pattern was initiated (using the protocol illustrated in Fig. 1), the results are qualitatively similar. The formation of an ordered, rotat-

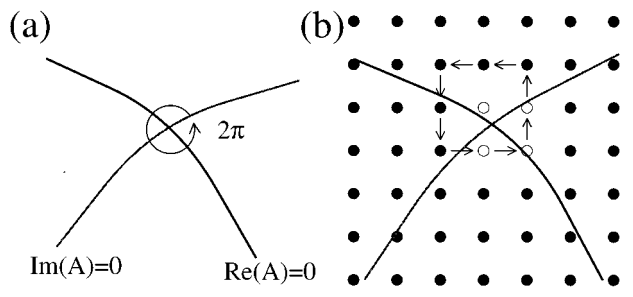

FIG. 14. Sketch of phase defects (a) in a continuous complex field, and (b) in a discrete complex field.

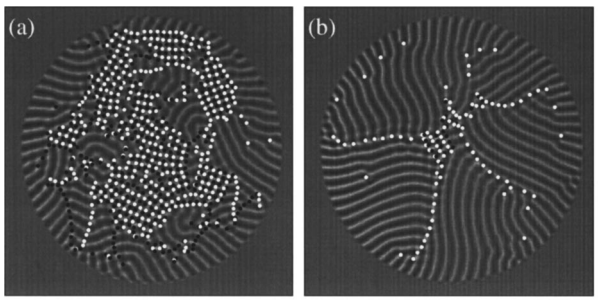

FIG. 16. Identification of phase defects in the patterns shown in Figs. 2(a) and 2(b). Defects of unit positive and negative topological charge are marked by white and black dots, respectively.

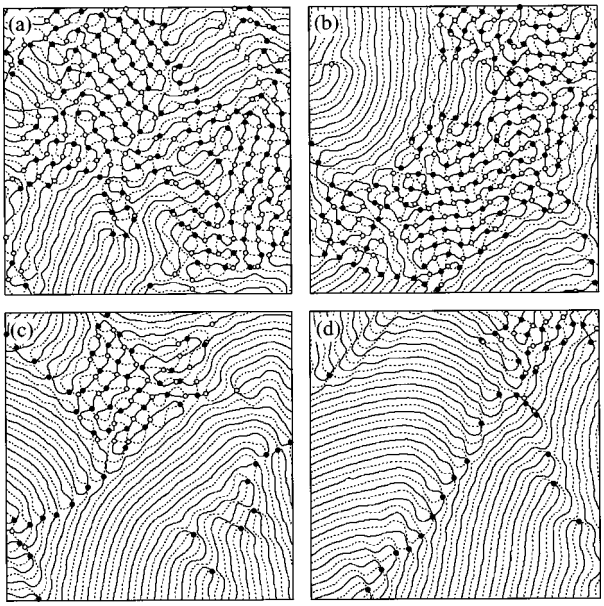

FIG. 17. Contours of $\mathrm{Re}(A)=0$ and $\mathrm{Im}(A)=0$ for an area near the center of the convection pattern. Positive (negative) defects are marked by closed (open) circles. The four patterns were recorded (a) 45τ, (b) 232τ, (c) 418τ, and (d) 697τ, after TW convection was initiated.

ing multidomain pattern is marked by an accumulation of net topological charge, followed by a rapid decrease in the number of defects. The net charge can only change due to defects entering the pattern from the boundary, whereas the decrease in the total number of charges occurs via the annihilation of pairs of oppositely charged defects within the pattern.

In Fig. 17, contours of $\mathrm{Re}(A)=0$ and $\mathrm{Im}(A)=0$ are shown for a different TW pattern which were created using the same protocol used for the pattern in Fig. 16. The four panels show an area at the center of the pattern, covering roughly half the area of the convection cell. Positive and negative phase defects are marked by filled and open dots. The trend is clear: as the pattern evolves, the knot of phase contours disentangles itself and evolves into a series of parallel lines which cross themselves the minimum number of times necessary to satisfy the external boundary conditions. These boundary conditions are mainly determined by the global rotation of the pattern and the tendency of the rolls to be oriented perpendicular to the cell boundary. The disentangling of the phase contours results in the annihilation of pairs of oppositely charged defects, leaving behind the excess charge.

B. Phase defects as a measure of disorder

An examination of Figs. 16 and 17 indicates that the ordering of the TW convection pattern is marked by a striking change in the topological structure of the complex order parameter. The disordered pattern has a very high density of phase defects, whereas the order parameter of the ordered pattern has a smooth phase distribution, with defects occurring only at domain boundaries. This suggests that the number of phase defects present in the pattern could be a good measure of the level of disorder.

We note that some care must be taken before identifying disorder with these phase defects. Most of the phase defects

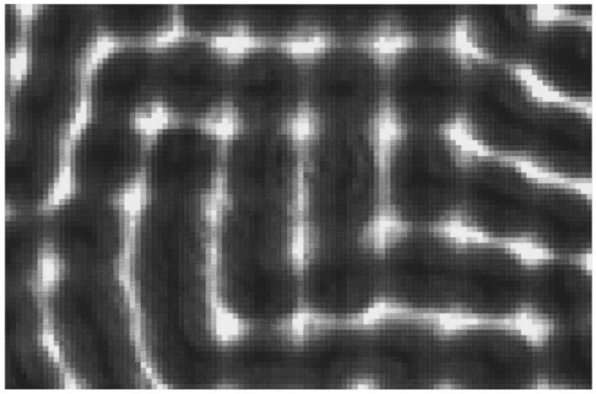

FIG. 18. A shadowgraph image of an area of a convection pattern containing a cross-roll pattern.

which are observed in the disordered patterns occur in the alternating cross-roll patches. If a uniform cross-roll pattern were stable, so that the four amplitudes in Eq. (20) were equal and independent of time and space, the alternating cross-roll pattern would consist of a perfect lattice of defects. In this case, a large number of defects with no net charge would be an indicator of *order* in the convection pattern. It is precisely because the cross-roll pattern is unstable and nonuniform that a large population of phase defects with net charge zero is an indicator of disorder in this system.

The instability of the alternating cross-roll pattern is implicit in the tendency of the patterns, which initially are rich in superpositions of wave components, to organize themselves into domains of pure traveling waves. This occurs because the dominant wave component within a superposition of waves tends to grow at the expense of the weaker components, until only a single-wave component remains. It is possible to directly measure the decay of the weaker wave component within a superposition of waves by studying domain boundaries, where there is a region of persistent wave interaction [41].

The nonuniformity of the cross-roll patterns may be confirmed by direct examination of a cross-roll pattern, and of its Fourier transform. Figure 18 shows an area of a convection pattern containing a well-defined alternating cross-roll pattern. The pattern exhibits significant nonuniformity. There is a tendency for different wave components to dominate in different parts of the pattern, which indicate fluctuations in the modulus of the wave component amplitudes. In addition, the alternation of horizontal and vertical rolls is not synchronized over the pattern, indicating phase fluctuations in these amplitudes. The four wave components of the cross-roll pattern can be identified in the Fourier transform of Fig. 18, which is shown in Fig. 19. The substantial spreading of the four main spectral peaks is a direct result of the nonuniformity of the pattern.

The net charge also has significance in understanding the evolution of the TW patterns. The convection rolls all have a perpendicular attachment to the unforced cell boundary, and each of these rolls terminates at a phase defect somewhere in the convection pattern—either at a domain boundary, a dislocation, or the edge of a cross-roll patch. Therefore, each roll attached to the boundary contributes a net charge of ± 1, depending on whether it is moving clockwise or counterclockwise around the cell boundary. (This may be con-

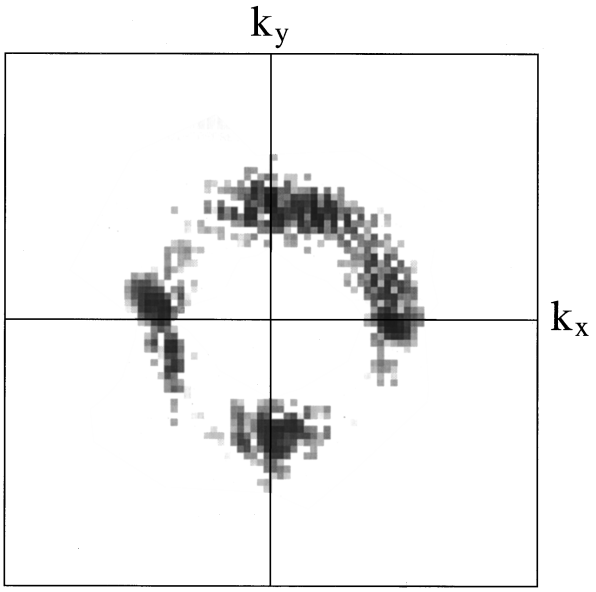

FIG. 19. The spatial Fourier transform of the cross-roll pattern shown in Fig. 18, where black indicates maximum spectral power.

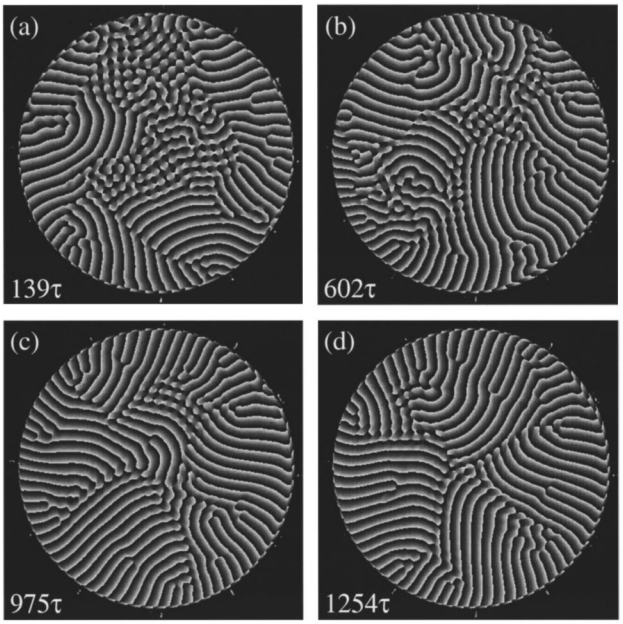

FIG. 20. The phase of the complex amplitude at several stages of the evolution of the pattern depicted in Fig. 2. The elapsed time since the initiation of convection is given for each of the four images.

firmed by examination of Fig. 16.) Rolls for which both ends are within the pattern have defects with opposite charge at either end and contribute no net charge. The wavelength of the pattern is quite rigid in this system, and there is room for 72 rolls around the boundary of the convection cell. The maximum net charge occurs when all of the rolls are moving in the same direction around the cell boundary, giving a charge of ± 72, where the sign depends on the direction of rotation. The net topological charge of the pattern is therefore an indicator of the global rotation of the pattern.

We may now use the net charge and the total number of defects to characterize the ordering of the TW convection patterns. Figures 20 and 21 show the complex order parameter and associated phase contours at four times during the coarsening of the pattern, and Fig. 22 shows the identification of phase defects from the corresponding panels in Fig. 20, in which positive and negative defects of unit charge are indicated by closed and open circles, respectively. The positions of the defects during the previous 23τ are shaded, indicating their trajectories. In Fig. 23, the number of defects and the net charge are plotted as a function of time for two runs during the coarsening of the patterns. The black curves are calculated from the pattern shown pictured in Figs. 16, 20, and 22, and the gray curves are calculated for another run conducted under nominally identical experimental conditions.

Figure 23 shows that the patterns initially have a large number of defects, with a net charge that is near zero. This indicates a substantial coverage by the disordered cross-roll pattern and no discernible global rotation. The pattern shown in Fig. 16(a) is in this stage of development. Within the first 100τ, there is a rapid ordering of the pattern, characterized by a decrease in the total number of defects, but no significant change in the net charge. In this stage traveling waves, either moving along the boundary or radiating from sources on the boundary, encroach on the disorder in the center of the pattern, causing a decrease in the area occupied by the cross-roll pattern. This initial ordering of the pattern does not lead directly to the highly ordered convection pattern observed at long times, but seems to stall with several hundred defects remaining. The ordering is arrested because cross-roll patches continue to be sustained in the center of the pattern by the collision of traveling-waves and because the sources, which appear on the boundary, are not stable. The pattern shown in Figs. 20(a) and 22(a) is recorded immediately after this initial ordering has occurred. This pattern contains a total of 553 defects and a net charge of $+19$, exhibiting a

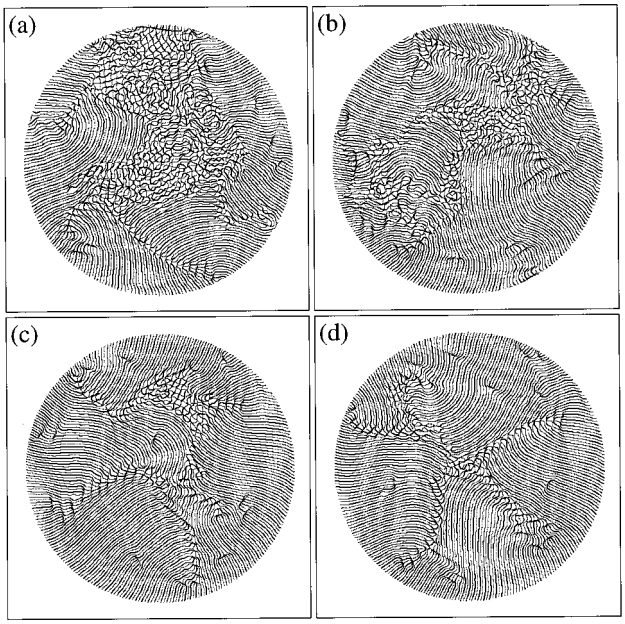

FIG. 21. Contours of $\mathrm{Re}(A)=0$ and $\mathrm{Im}(A)=0$ are marked by black and gray lines for the patterns shown in the four panels of Fig. 20.

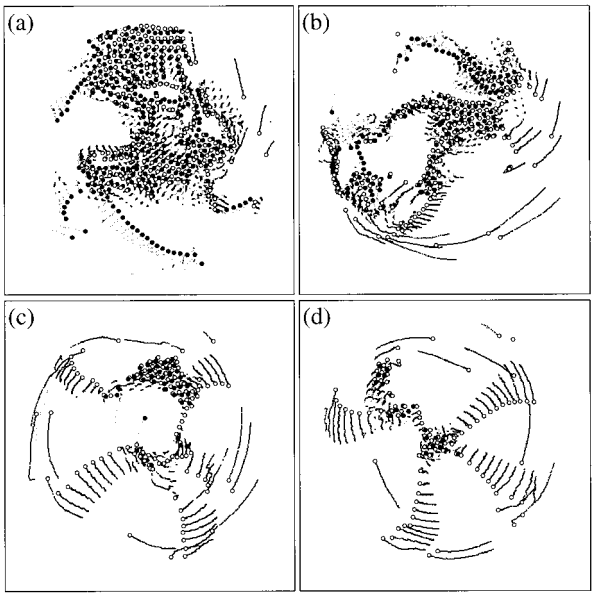

FIG. 22. Defect identification for the four panels of Fig 20. Positive (negative) defects are marked by closed (open) circles and the positions of positive (negative) defects over the previous 23τ are shaded in light (dark) gray.

substantial coverage by the cross-roll patches, but no significant rotation. This is apparently the highest level of order that can be achieved in a nonrotating pattern.

Returning to Fig. 23, the net charge steadily accumulates during the period from 100τ to about 500τ, while the total number of defects remains high, signaling that the patterns are developing a sense of rotation, while remaining largely disordered. The pattern shown in Figs. 20(b) and 22(b) is recorded near the end of this period of persistent disorder, and has 321 defects with a net charge of -27. Examination of the rolls near the boundary of the pattern in Fig. 20(b) reveals that about two-thirds of the rolls are moving in the clockwise direction, indicating that clockwise rotation is beginning to dominate. In Fig. 22(b) negative defects (open circles) can be seen entering the pattern from the cell boundary, particularly in the dislocations originating on the right side of the cell and in the small, poorly formed zipper boundary which is moving in from the far left.

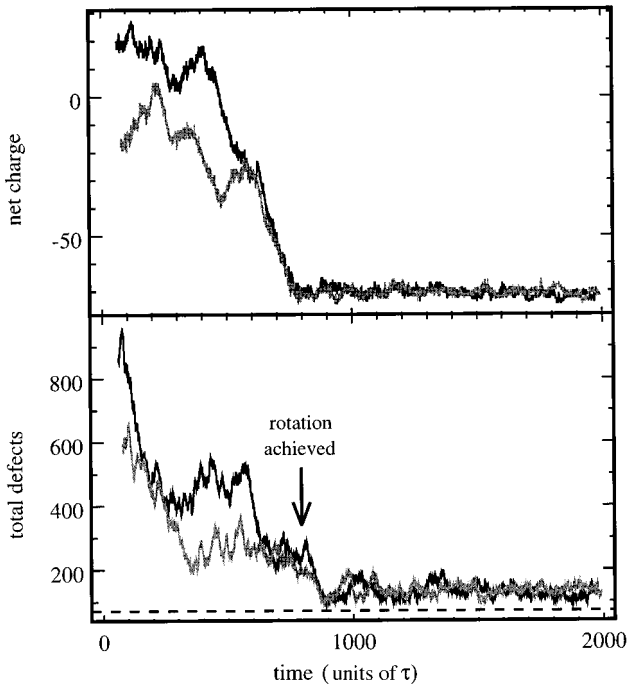

FIG. 23. Statistics of phase defects as a function of time for two convection patterns created under identical experimental conditions. The black curve is the same run shown in Figs. 16, 20, and 22. The dashed line in (b) represents the minimum level of -72 defects.

The pattern continues to accumulate net charge and, at time 800τ, it reaches the limiting value of -72, indicating that the globally rotating pattern has fully formed. This is immediately followed by an almost total collapse of the number of defects in the pattern. Figs. 20(c) and 22(c) show the pattern shortly after this transition has occurred. At this point, the pattern has 156 defects and a net charge of -70. From this time onward, the number of defects is remarkably stable, with a net charge remaining at -71 ± 1 and with the total number of defects varying between 100 and 150. Figures 20(d) and 22(d) show a particularly well-ordered pattern from this final stage of the coarsening process.

Although the nature of the patterns depends sensitively on the Rayleigh number, the ordering process seems to be essentially the same over a broad range of Rayleigh numbers near r_s, where perpendicular or zipper domain boundaries predominate [32]. The ordering of the pattern begins immediately, but stalls with 300–500 defects remaining, while the net charge of the pattern steadily accumulates. When the limiting net charge of ±72 is reached, there is a rapid decrease in the number of defects, suggesting that the ordering mechanism is facilitated by the state of global rotation. At higher values of the Rayleigh number (nearer to $r^\star$) the domain boundaries contained in the patterns become pinned, and the patterns are a composite of traveling and stationary rolls. In this regime, the pattern dynamics are qualitatively different, and the analysis techniques described here, which depend on the oscillatory nature of the pattern, cannot be used.

The process by which the pattern orders itself is also critically dependent on the boundary conditions at the sidewall of the convection cell. Because of its physical construction, the sidewall of the convection cell is thermally neutral [32], which causes the convection rolls to be oriented perpendicular to this boundary. Also, because the radius of curvature of the circular cell boundary is much larger than the roll wavelength, sources on the cell boundary (wall foci) are unstable. The globally rotating patterns are consistent with these two conditions, since they allow for the perpendicular orientation of the rolls and do not require sources on the boundary. A mixed rotation pattern, with domains of rolls moving in different directions around the cell boundary, implies the presence of sources and sinks at the boundary, which are not found to be stable and break down into disordered structures. The fact that sources on the boundary are unstable has a profound influence on the development of the patterns. Our

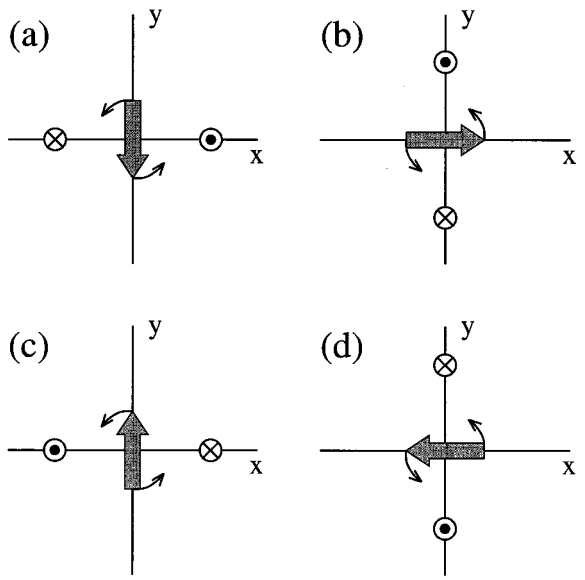

FIG. 24. Schematic representation of the vertical component of the velocity field (v_z) for a defect at the origin ($x=y=0$). The dot represents upflow, the cross represents downflow and the gray arrow indicates the direction of the vorticity at times (a) $\pi/4\omega$, (b) $\pi/2\omega$, (c) $3\pi/4\omega$, and (d) π/ω. The vorticity precesses at the temporal oscillation frequency, ω.

experiments in a rectangular convection cell (not shown) indicate that a stable source can form in a corner of the cell. In this case, the source launches stable waves into the pattern, which leads to a rapid ordering *without* global rotation.

C. Physical significance of the phase defects

An important issue is what physical significance, if any, can be attributed to the phase defects in the TW patterns. In many contexts, the topologically charged phase defects such as those described here are called vortices [6]. This is an appropriate interpretation in cases where the gradient of the order parameter is a current, so that the phase defects are associated with current loops. An example of such a case is the Ginzburg-Landau theory of superconductivity, where the gradient of the order parameter is the supercurrent, and the current loop associated with the phase defect confines a tube of magnetic flux.

In the experiment described here, the shadowgraph visualization system is sensitive to fluctuations in the fluid density, which are closely correlated with the temperature and with the vertical component of the fluid velocity near the midplane of the convection cell. Since the order parameter is associated with the vertical component of the fluid velocity, the phase defect is not directly associated with the vertical vorticity in the fluid. In fact, the phase defect indicates the presence of horizontal vorticity that precesses about the vertical axis, as illustrated in Fig. 24. Near the defect, the vertical component of the velocity is of the form

$$u_z(x,y,t)=\mathrm{Re}[u(r)e^{i(\theta-\omega t)}], \tag{21}$$

where r is the distance from the defect core and θ is the polar angle in the standard cylindrical coordinates. The function $u(r)$ goes to zero at $r=0$, where the phase is undefined. At $t=0$, u_z is positive for positive $x>0$ and negative for $x<0$, and the connection of the flow lines above and below the midplane of the fluid layer imply vorticity in the negative y direction. At time $t=\pi/4\omega$, the flow field has rotated, so that u_z is positive for $y>0$ and negative for $y<0$ and the vorticity is along x. In general, the vorticity at the phase defect core rotates in the horizontal plane at frequency ω.

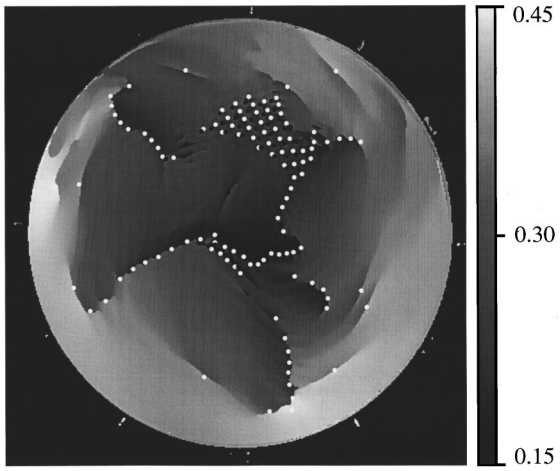

FIG. 25. Frequency field calculated from the pattern shown in Fig. 20(c). Phase defects of positive (negative) charge are marked with black (white) dots. The frequency is in units of the vertical diffusion time and is mapped to grayscale according to the legend.

The existence of traveling waves in binary fluid convection depends sensitively on the development of a phase shift between the temperature and concentration fields, which has been shown to occur in simulations of two-dimensional TW convection [28]. This breaking of symmetry has also been observed in quasi-two-dimensional convective flows in restricted geometries [45,46]. Presumably, a similar flow would develop in the large domains of traveling waves in patterns studied here. As described above, phase defects correspond to points in the pattern where the flow is very complicated, and it is plausible that this could interfere with the delicate interaction of temperature and concentration in the TW state.

There is experimental evidence that TW convection is modified in the neighborhood of the phase defects. In Fig. 25, the temporal oscillation frequency is shown as a function of position for a pattern containing large domains of traveling waves, as well as some concentrations of defects. This frequency field was calculated using an algorithm we have described elsewhere [32]. A significant suppression of the oscillation frequency is observed in the vicinity of the phase defects. Figure 26 is a histogram of the frequency data shown in Fig. 25. It is clear from this histogram that the oscillation frequency and therefore the phase velocity is significantly lower near the defects than in regions of pure traveling waves. This suppression of the frequency is consistent with a decrease in the effective separation ratio in the vicinity of the phase defects.

VI. INTERACTION OF DEFECTS

In Sec. V, it was shown that the phase defects are an effective measure of disorder in the TW convection patterns.

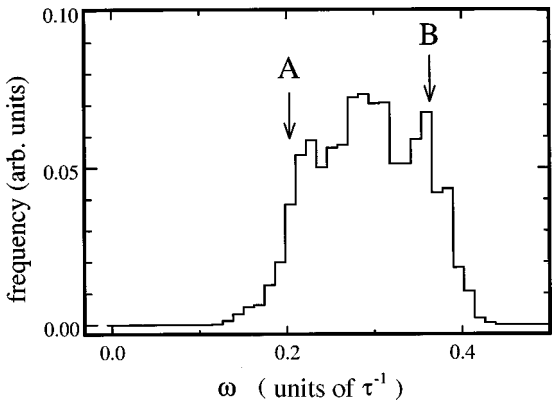

FIG. 26. Histogram of the frequency field shown in Fig. 25. *A* indicates the frequency close to the phase defects, and *B* indicates the frequency far from the phase defects.

It is possible to go one step further and ask if the dynamics of the defects and particularly their interaction with each other, are significant in determining the development of the pattern. The most basic way to address this question is to measure the defect-defect correlation functions.

In order to measure these correlations, the complex order parameter is first calculated as a function of time and space for a high-resolution video sequence, such as the one shown in Fig. 17. For each frame, a list is compiled of the charge and position of each defect. The correlation functions are then calculated using the formulas

$$C_{pp}=\frac{1}{N_{pp}}\sum_{m\neq n}\delta_{(x_n-x_m-x)}\delta_{(y_n-y_m-y)}\delta_{(c_n-c_m)},$$
$$C_{pn}=\frac{1}{N_{pn}}\sum_{m\neq n}\delta_{(x_n-x_m-x)}\delta_{(y_n-y_m-y)}\delta_{(c_n+c_m)}, \tag{22}$$

where $C_{pp}(x,y)$ is the correlation between defects of like sign, and $C_{pm}(x,y)$ is the correlation between defects of unlike sign. In these formulas, the summations are over all pairs of defects in a given frame, (x_n,y_n) are the integer coordinates and c_n is the charge of the n^{th} defect. The symbol $\delta_{(n)}$ is defined to be one when $n=0$ and zero otherwise. The correlations are normalized to the number of defects and indicate the probability that a defect has a neighbor of the specified sign at a given displacement. The correlation functions are calculated averaging over as many frames as necessary to obtain adequate statistics.

The like- and unlike-sign correlation functions (C_{pp} and C_{pn}), calculated for a disordered convection pattern, are shown in Figs. 27 and 28, respectively. The data are averaged over approximately 300τ and are calculated from defects in the central region of the convection pattern, so that the cell boundary is not an important influence on the motion of the defects. Most of the defects in the pattern appear in an extended cross-roll patch, so that the correlation function mainly reflects the periodicity of the lattice of defects in the cross-roll pattern (see Fig. 13). Since the ordering of the pattern is closely related to the instability of the cross-roll pattern, these correlation functions may give some insight into the ordering mechanism.

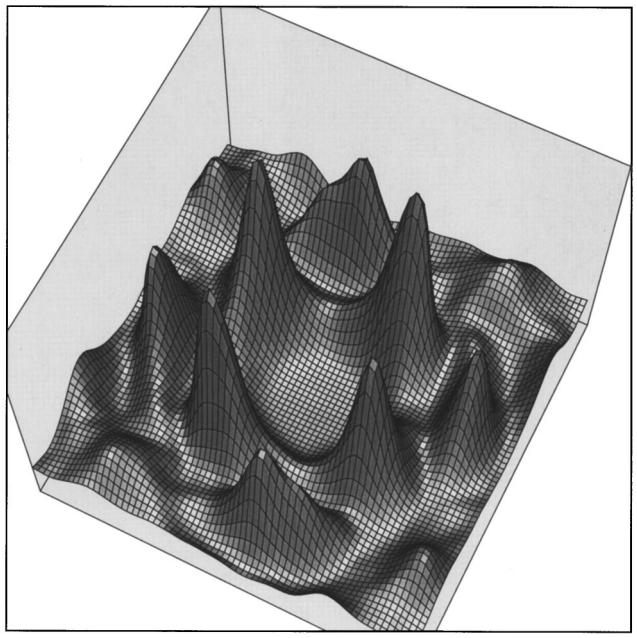

FIG. 27. Like-sign defect-defect correlation function (C_{pp}) for a disordered TW convection pattern.

In the like-sign correlation function, C_{pp}, shown in Fig. 27, there are four large peaks arising from the nearest like-sign neighbors, as well as smaller peaks arising from more distant neighbors. In the unlike-sign correlation function, C_{pn}, shown in Fig. 28, there are again four peaks corresponding to nearest neighbors.

The radial distributions of the correlation functions are plotted in Fig. 29. Both functions approach the same asymptotic value at large separations, but are dramatically different at small separations. The distribution of C_{pp} exhibits peaks at $\sqrt{2}h$ and at $2h$, indicating a tendency for like-

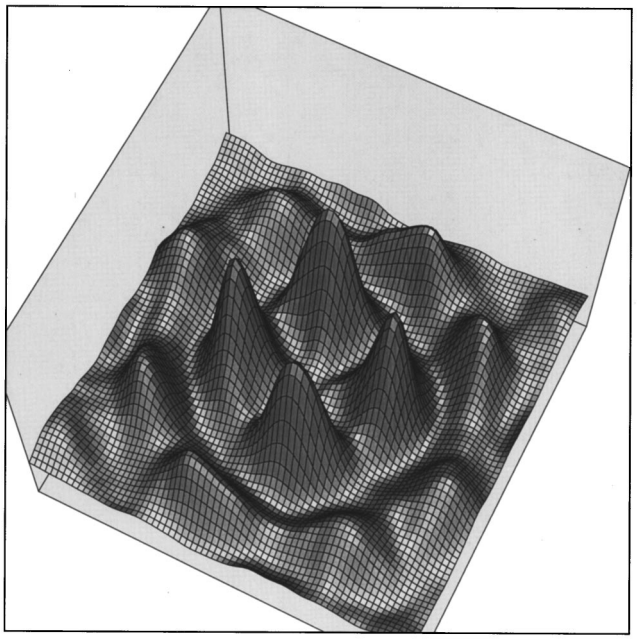

FIG. 28. Unlike-sign defect-defect correlation function (C_{pn}) for a disordered TW convection pattern.

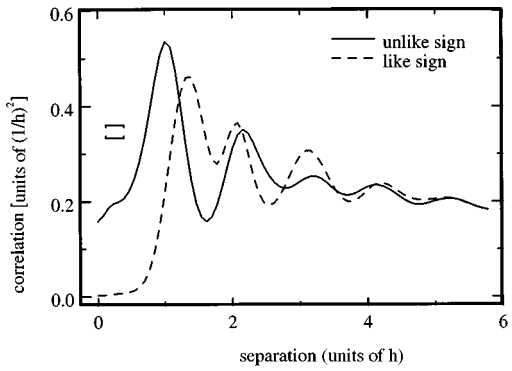

FIG. 29. The radial distribution of the defect-defect correlation function. The dashed line indicates like-sign correlation (C_{pp}), and the solid line indicates unlike-sign correlation (C_{pn}).

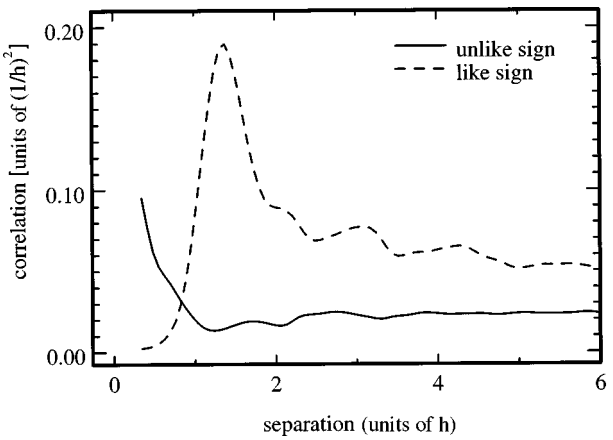

FIG. 30. The radial distribution of the conditional defect-defect correlation function (from which defects within cross-roll patches are excluded) as described in the text. The dashed line indicates the like-sign correlation (C_{pp}), and the solid line indicates the unlike-sign correlation (C_{pn}).

sign defect pairs to maintain these separations. The most significant aspect of C_{pp} is the fact that it goes to zero as the displacement approaches zero, indicating that defects of like sign never approach each other, so that there is an effective hard-core repulsion among defects of like sign. The distribution of C_{pn} has peaks at h and $\sqrt{5}h$. The distribution of C_{pn} has a finite value at zero displacement, suggesting that there is no repulsion between defects of opposite sign at short range, but that the defects tend to sit at a finite separation.

The defect-defect interactions implied by the measured defect correlation functions can be related to some of the basic features of the disordered convection patterns. The ability of unlike-sign defects to approach each other allows annihilation to occur and facilitates the ordering of the patterns. The inability of like-sign defects to approach each other prevents the formation of multiply charged defect structures, such as multiarmed spirals.

It is important to determine the extent to which the correlation functions measured in the disordered patterns are intrinsic properties of the phase defects, rather than merely a reflection of the periodic nature of the cross-roll pattern. One way to address this question is to see if the correlation functions measured in the disordered patterns are consistent with the behavior of the defects in the ordered patterns.

Figure 30 shows defect-defect correlation functions compiled from a period of 350τ during the evolution of an ordered convection pattern, such as those shown in Figs. 2(b) and 20(d). During the video sequence, the pattern consists mainly of large domains of traveling waves separated by nominally perpendicular domain boundaries, along with small, transient cross-roll patches. Even though the cross-roll pattern fills a relatively small area of the pattern, it contains a high density of defects, and tends to dominate the defect-defect correlations, even in the ordered patterns. In an attempt to measure the ''bare'' defect interactions, a conditional probability distribution was calculated, in which defects are excluded if they have six or more neighbors within a radius of $2h$. This condition excludes defects in cross-roll patches, for which 12 neighbors are expected, but includes defects in domain boundaries, dislocation, or in small ensembles of defects. Comparison of the correlation functions in Figs. 29 and 30 helps to distinguish between bare defect interactions and the ensemble interactions which occur in the cross-roll pattern.

At small separation, the like-sign correlation function C_{pp} in Fig. 30 resembles that of Fig. 29, rising from a value of zero at zero separation, to a maximum near separation $\sqrt{2}h$, although the smaller peaks at larger separation are absent in Fig. 30. In the ordered pattern, like-sign defects still exhibit hard-core repulsion and the tendency to sit at spacing of $\sqrt{2}h$, which was found for the disordered patterns, and these appear to be intrinsic properties of the phase defects.

However, the unlike-sign correlation function C_{pn} in Fig. 30 is very different from that shown in Fig. 29. In Fig. 30, C_{pn} has a shallow dip at separations near h, and rises to a maximum for zero separation, exhibiting no peaks at finite separation. The dip in C_{pn} at small nonzero separation suggests that defects which come within range are drawn together and annihilate. This is consistent with the observed motion of the defects in the ordered patterns. The large peaks in C_{pn} observed in Fig. 29 (which suggest that oppositely charged defects could form bound pairs) are apparently specific to the cross-roll pattern, and are not applicable to defects in isolation.

VII. CONCLUSION

In this paper we considered the coarsening of a traveling-wave convection pattern, that is to say, the transition from a disordered pattern to a ordered one. This transition is not marked by a dramatic change in the spatial Fourier spectrum or the spatial autocorrelation function of the patterns. Both ordered and disordered patterns are comprised of a continuous spectrum of wave vectors, which spans all directions, but a narrow range of $|\mathbf{k}|$. In the disordered patterns, the wave components with differing directions overlap, whereas, in the ordered pattern, they are segregated into individual domains of traveling waves. The ordering of the patterns does not, as one might have expected, consist of a dramatic sharpening of the wave number spectrum, or increase of long-range order, as measured by linear correlations or mutual information. In the frequency domain, the ordering of the pattern apparently corresponds to the formation of complicated phase relationships among the Fourier components.

The most important results of this study are twofold: we can extract the complex order parameter from experimental TW patterns, and the coarsening of the patterns is associated with a dramatic change in the topological structure of this order parameter. The disordered patterns contain a large number of singularities in the phase of the order parameter, with phase defects of positive and negative topological charge occurring in roughly equal numbers. As the patterns coarsen and domains of traveling waves suppress the superpositions of wave components, pairs of oppositely charged defects annihilate, leaving behind a much smoother phase field. The defects which remain form linear arrays of like-sign defects, which correspond to boundaries between domains of traveling waves. At the same time, a buildup of net charge occurs due to a charge imbalance between defects entering and leaving the pattern at the system boundary. The accumulation of this net charge corresponds to the development of global rotation in the pattern. We conclude that the total number and net charge of the population of defects are very direct measures of the level of disorder in the system.

Another important question is whether it is possible to elevate the phase defects from their role as mere indicators of the pattern dynamics to a role of *determining* the dynamics of the patterns. In spatially extended dissipative systems, the organization of a pattern is often associated with the formation of coherent structures. In an idealized, homogeneous Rayleigh-Bénard convection pattern, the convection rolls themselves are the primary coherent structures. In the very complicated convection patterns studied in this paper, it is possible that the defects in the pattern might be regarded as the central ''coherent structures'' in the system, and that the development of the pattern can be interpreted as resulting from the interaction of these defects with the underlying wave field and with each other.

The latter part of this paper begins to address this issue. Figure 22 illustrates the relationship between the defects and the wave field, with defects remaining stationary within the alternating cross-roll patches, slowly drifting in domain boundaries, and being swept along with the waves in dislocations. The correlation functions shown in Figs. 27 and 28 address the interaction of the defects with each other, and suggest that there may be an effective defect-defect interaction potential which exerts a strong influence on the development of the patterns. While the calculation of the defect correlation functions is only the crudest measure of defect-defect interactions, the ability to track the trajectories of phase defects in this system leaves open the possibility of doing more in-depth studies of the defect dynamics.

Finally, to take a more general view, complex amplitude fields containing phase singularities are used to describe a variety of physical systems. In the Ginzburg-Landau theory of superconductivity, flux vortices are described using an identical formalism, and the lattice of defects in a alternating cross-roll pattern makes an interesting comparison with the Abrikosov flux lattice. Similar vortex structures were also studied in superfluid helium, in optical resonators [6,7,14,47,48] and in reaction-diffusion systems [49]. The traveling-wave convection system studied here is particularly attractive because in this system it is possible to directly measure the dynamics of the complex order parameter in an experiment containing a large number of phase defects.

ACKNOWLEDGMENTS

We would like to acknowledge useful discussions with M. C. Cross, H. Greenside, T. Hwa, D. Ridgway, and H. Riecke. This work was supported by the U. S. Department of Energy under Grant No. DE-FG03-90ER14148.

[1] M. C. Cross and P. C. Hohenberg, Rev. Mod. Phys. **65**, 851 (1993).
[2] P. Manneville, *Dissipative Structures and Weak Turbulence* (Academic, Boston, 1990).
[3] J. D. Murray, *Nonlinear Differential Equation Models in Biology* (Clarendon, Oxford, 1977).
[4] J. J. Bonner, *The Cellular Slime Molds* (Princeton University Press, Princeton, NJ, 1967).
[5] W. F. Loomis, *Dictyostelium Discoidium, A Developmental System* (Academic, New York, 1975).
[6] P. Coullet, L. Gil, and F. Rocca, Opt. Commun. **73**, 403 (1989).
[7] K. Staliunas, Phys. Rev. A **48**, 1573 (1993).
[8] J. Lega, J. V. Moloney, and A. C. Newell, Phys. Rev. Lett. **73**, 2978 (1994).
[9] V. Steinberg, W. Moses, and J. Fineberg, Nucl. Phys. B **2**, 109 (1987).
[10] P. Kolodner, J. A. Glazier, and H. Williams, Phys. Rev. Lett. **65**, 1579 (1990).
[11] Y. Hu, R. E. Ecke, and G. Ahlers, Phys. Rev. Lett. **74**, 5040 (1995).
[12] I. Rehberg, S. Rasenat, and V. Steinberg, Phys. Rev. Lett. **62**, 756 (1989).
[13] S. W. Morris, E. Bodenshatz, D. S. Cannell, and G. Ahlers, Phys. Rev. Lett. **71**, 2026 (1993).
[14] F. T. Arecchi, G. Giacomelli, P. L. Ramazza, and S. Residori, Phys. Rev. Lett. **67**, 3749 (1991).
[15] C. S. Bretherton and E. A. Spiegel, Phys. Lett. **96A**, 152 (1983).
[16] D. Kazhdan, L. Shtilman, A. A. Golovin, and L. M. Pismen, Phys. Fluids **7**, 2679 (1995).
[17] P. Coullet, C. Elphick, L. Gil, and J. Lega, Phys. Rev. Lett. **59**, 884 (1987).
[18] H. Xi, J. D. Gunton, and J. Vinals, Phys. Rev. Lett. **71**, 2030 (1993).
[19] D. A. Egolf and H. S. Greenside, Phys. Rev. Lett. **74**, 1751 (1995).
[20] B. W. Roberts, E. Bodenschatz, and J. P. Sethna, Physica D **99**, 252 (1996).
[21] L. D. Landau and E. M. Lifshitz, *Fluid Mechanics*, 2nd ed. Course of Theoretical Physics Vol. 6 (Pergamon, Oxford, 1987).
[22] J. K. Platten and J. C. Legros, *Convection in Liquids* (Springer-Verlag, Berlin, 1984).
[23] B. J. A. Zielinska and H. R. Brand, Phys. Rev. A **35**, 4349 (1987).

[24] M. C. Cross and K. Kim, Phys. Rev. A **38**, 529 (1988).
[25] E. Knobloch and D. R. Moore, Phys. Rev. A **37**, 860 (1988).
[26] P. Kolodner, H. Williams, and C. Moe, J. Chem. Phys. **88**, 6512 (1988).
[27] W. Barten, M. Lücke, W. Hort, and M. Kamps, Phys. Rev. Lett. **63**, 376 (1989).
[28] M. Lücke, W. Barten, and M. Kamps, Physica D **61**, 183 (1992).
[29] W. Barten, M. Lücke, M. Kamps, and R. Schmitz, Phys. Rev. E **51**, 5636 (1995).
[30] D. R. Ohlsen, S. Y. Yamamoto, C. M. Surko, and P. Kolodner, Phys. Rev. Lett. **65**, 1431 (1990).
[31] A. La Porta, K. D. Eaton, and C. M. Surko, Phys. Rev. E **53**, 570 (1996).
[32] A. La Porta and C. M. Surko, Phys. Rev. E **53**, 5916 (1996).
[33] Y. Hu, R. E. Ecke, and G. Ahlers, Phys. Rev. Lett. **74**, 391 (1995).
[34] C. E. Shannon and W. Weaver, *The Mathematical Theory of Communication* (University of Illinois Press, Urbana, IL, 1949).
[35] A. M. Fraser and H. L. Swinney, Phys. Rev. A **33**, 1134 (1986).
[36] A. M. Fraser, IEEE Trans. Inf. Theory **35**, 245 (1989).
[37] P. Kolodner, C. M. Surko, and H. Williams, Physica D **37**, 319 (1989).
[38] P. Kolodner and H. Williams, in *Nonlinear Evolution of Spatio-Temporal Structures in Dissipative Continuous Systems*, edited by F. H. Busse and L. Kramer (Plenum, New York, 1990), pp. 73–91.
[39] R. W. Walden, P. Kolodner, A. Passner, and C. M. Surko, Phys. Rev. Lett. **55**, 496 (1985).
[40] I. Aranson and L. Tsimring, Phys. Rev. Lett. **75**, 3273 (1995).
[41] A. La Porta and C. M. Surko, Phys. Rev. E **55**, 6327 (1997).
[42] A. C. Newell, T. Passot, and J. Lega, Annu. Rev. Fluid Mech. **25**, 399 (1993).
[43] M. Silber and E. Knobloch, Nonlinearity **4**, 1063 (1991).
[44] A. La Porta and C. M. Surko, Phys. Rev. Lett. **77**, 2678 (1996).
[45] B. L. Winkler and P. Kolodner, J. Fluid Mech. **240**, 31 (1992).
[46] K. D. Eaton *et al.*, Phys. Rev. A **43**, 7105 (1991).
[47] F. T. Arecchi, S. Boccaletti, P. L. Ramazza, and S. Residori, Phys. Rev. Lett. **70**, 2277 (1993).
[48] K. Staliunas and C. O. Weiss, Physica D **81**, 79 (1995).
[49] I. Aranson, H. Levine, and L. Tsimring, Phys. Rev. Lett. **76**, 1170 (1996).